PCCP

PAPER

View Article Online
View Journal | View Issue

Cite this: *Phys. Chem. Chem. Phys.*, 2023, **25**, 29516

Tetracoordinate Co(II) complexes with semi-coordination as stable single-ion magnets for deposition on graphene†

Jorge Navarro Giraldo, [a] Jakub Hrubý, ‡[a] Šárka Vavrečková,§[ab] Ondřej F. Fellner, [c] Lubomír Havlíček, [ad] DaVonne Henry,[e] Shehan de Silva,[e] Radovan Herchel, [c] Miroslav Bartoš,[a] Ivan Šalitroš, [af] Vinicius T. Santana,[a] Paola Barbara, [e] Ivan Nemec *[ac] and Petr Neugebauer *[a]

We present a theoretical and experimental study of two tetracoordinate Co(II)-based complexes with semi-coordination interactions, *i.e.*, non-covalent interactions involving the central atom. We argue that such interactions enhance the thermal and structural stability of the compounds, making them appropriate for deposition on substrates, as demonstrated by their successful deposition on graphene. DC magnetometry and high-frequency electron spin resonance (HF-ESR) experiments revealed an axial magnetic anisotropy and weak intermolecular antiferromagnetic coupling in both compounds, supported by theoretical predictions from complete active space self-consistent field calculations complemented by N-electron valence state second-order perturbation theory (CASSCF-NEVPT2), and broken-symmetry density functional theory (BS-DFT). AC magnetometry demonstrated that the compounds are field-induced single-ion magnets (SIMs) at applied static magnetic fields, with slow relaxation of magnetization governed by a combination of quantum tunneling, Orbach, and direct relaxation mechanisms. The structural stability under ambient conditions and after deposition was confirmed by X-ray photoelectron spectroscopy (XPS) and Raman spectroscopy. Theoretical modeling by DFT of different configurations of these systems on graphene revealed n-type doping of graphene originating from electron transfer from the deposited molecules, confirmed by electrical transport measurements and Raman spectroscopy.

Received 29th March 2023,
Accepted 3rd October 2023

DOI: 10.1039/d3cp01426f

rsc.li/pccp

1 Introduction

Hybrid materials combining single-molecule magnets (SMMs) and solid-state materials are attractive candidates for next-generation technologies, such as high-density magnetic memory devices,[1] qubits,[2] and spintronic devices.[3–5] The solid-state substrate, having metallic, semi-metallic, or insulating character, provides a platform for the deposition of SMMs in the form of thin films, allowing addressing or manipulation of the molecular magnetic and electric properties.[4,6,7] For their successful deposition, the molecular compounds must present an increased chemical, structural, and thermal stability that guarantees the preservation of their magnetic properties during and after the deposition process,[4] which often involves their sublimation at high temperatures and under high-vacuum conditions. These features pose considerable challenges to the design of sublimable SMMs, such that the number of demonstrated complexes suitable for deposition and spintronic applications remains small.[4]

Co(II)-based coordination compounds often exhibit interesting magnetic properties emerging from a large spin–orbit coupling

[a] *Central European Institute of Technology, CEITEC BUT, Purkyňova 656/123, 61200 Brno, Czech Republic. E-mail: ivan.nemec@ceitec.vutbr.cz, petr.neugebauer@ceitec.vutbr.cz*
[b] *Institute of Physical Engineering, Faculty of Mechanical Engineering, Brno University of Technology, Technická 2, 61669 Brno, Czech Republic*
[c] *Department of Inorganic Chemistry, Faculty of Science, Palacký University, 17. listopadu 12, 77147 Olomouc, Czech Republic*
[d] *Institute of Physics of Materials, Czech Academy of Sciences, Žižkova 22, 61662 Brno, Czech Republic*
[e] *Department of Physics, Georgetown University, Washington, DC, USA*
[f] *Department of Inorganic Chemistry, Faculty of Chemical and Food Technology, Slovak University of Technology in Bratislava, Bratislava SK-81237, Slovakia*

† Electronic supplementary information (ESI) available. See DOI: https://doi.org/10.1039/d3cp01426f

‡ Present address: National High Magnetic Field Laboratory, Florida State University, 1800 E. Paul Dirac Drive Tallahassee, FL 32310, USA.
§ Present address: Institute of Applied Physics, Abbe Center of Photonics, Friedrich Schiller University, Albert-Einstein-Str. 15, 07745 Jena, Germany.

(SOC) inducing very large magnetic anisotropies in certain ligand field symmetries. For the preparation of SMMs, or their analogs with only one paramagnetic center, single-ion magnets (SIMs), it is important for the molecule to possess a large and preferably axial type of magnetic anisotropy ($D < 0$), which is usually observed for low coordinate Co(II) complexes such as dicoordinate,[8] tetracoordinate,[9–13] pentacoordinate,[14–20] but also hexacoordinate with trigonal ligand field symmetry.[21–27] To date, the most extensively investigated group of Co(II) SIMs consists of tetracoordinate complexes.[28,29] Within this class, the most intriguing results have been observed for SIMs that exhibit slow relaxation of magnetization in zero external magnetic fields, commonly known as zero-field SIMs (ZF-SIMs). There are only two groups of tetracoordinate Co(II) ZF-SIMs: those composed of monodentate ligands with S, Se, or Te donor atoms,[30–32] and those formed by bidentate ligands that create acute bite angles.[33–37] Our previous investigations strongly suggest avoiding the use of monodentate ligands in complexes intended for thermal depositions. Recently, we attempted to deposit two different types of tetracoordinate Co(II) complexes on various substrates, but found that the stability of the complex molecules during deposition was problematic under ambient conditions.[38] Even the use of a protective atmosphere was not sufficient to deposit intact tetracoordinate Co(II) molecules.[39] To enhance the stability of the Co(II) complexes intended for depositions we opted to use bidentate ligands instead of monodentate ligands. We decided to use bidentate Schiff base ligands which are well known for forming mononuclear Co(II) complexes exhibiting field-induced or zero-field slow relaxation of magnetization. Furthermore, we modified the Schiff base ligands by adding a 2-pyridyl substituent to ensure the high stability of the molecular complexes. This provides an additional nitrogen atom that is sterically hindered from forming a regular coordination bond with the metal atom. However, it can form a non-covalent interaction with the adjacent metal center. As we recently proposed,[40] non-covalent interactions between the donor atoms possessing free electron pairs such as N or O, and metal atoms can enhance the stability of the molecular complex without affecting the magnetic anisotropy of the metal centers significantly. Therefore, for depositions, we decided to utilize Co(II) compounds with a specific class of Schiff base ligands derived from the condensation of aromatic 2-hydroxo-benzaldehydes and 2-amino-6-picoline. The crystal structure of the Co(II) compound with the Hsalapi ligand (Hsalapi = 2-methyl-6-(2′-oxybenzylideneamino)pyridin) was reported previously.[41] In its crystal structure (Cambridge Structural Database code MIFWUU),[42] we see that two deprotonated salapi$^-$ ligands coordinate the Co(II) atom in a bidentate manner giving rise to the [Co(salapi)$_2$] molecule (Fig. 1). Remarkably, the pyridine nitrogen atoms point towards the metal center, but the Co···N distances are relatively long (2.625(14) and 2.708(14) Å). Thus, from the perspective of structural coordination chemistry, these contacts could be classified as semi-coordinative because of their non-covalent nature and major electrostatic contribution.[43–48]

In this work, we opted to investigate whether the [Co(salapi)$_2$] (hereafter **1**) and structurally related [Co(me-salapi)$_2$] (hereafter **2**, Hme-salapi = 2-methyl-6-(2′-oxy-4′-methyl-benzylideneamino)-pyridin) molecules can be magnetically considered to be tetracoordinate despite having relatively short Co···N non-covalent interactions. Furthermore, we investigated whether the Co···N interactions are stabilizing structures of molecules in **1** and **2** sufficiently enough for their utilization in depositions by wet chemistry and thermal sublimation. In this case, we performed molecular deposition on commercially available single-layer graphene.[49] Graphene offers interesting properties such as high electron mobility, spin transport, mechanical strength, and thermal conductivity.[50–53] Furthermore, in our vision, graphene serves as a good substrate for deposition when nanostructured into a quantum dot, which could be used as a bolometer for *in situ* spectroscopy of deposited compounds.[54,55] Graphene could also be used for the electrical addressing of SMMs, as it can be shaped and utilized for graphene transistors[56] that are commercially available nowadays.

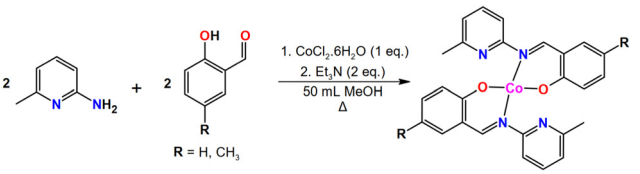

Fig. 1 Preparation scheme of compounds 1 (Co(salapi)$_2$, R = H) and 2 (Co(me-salapi)$_2$, R = CH$_3$).

Herein, we report on the synthesis, crystal structure, magnetic properties, and characterization of compounds **1** and **2** along with a theoretical study of their semi-coordination aspects, magnetic properties, and intermolecular exchange interactions. Direct current (DC) magnetometry and HF-ESR measurements demonstrated that the compounds present an axial magnetic anisotropy and a weak intermolecular antiferromagnetic exchange interaction, corroborated by broken-symmetry DFT (BS-DFT) calculations; while alternating current (AC) magnetometry showed that both compounds behave as field-induced SIMs. We also carried out a successful deposition of **1** and **2** on graphene and compared the results to a bulk reference. Raman spectroscopy, X-ray photoelectron spectroscopy (XPS), atomic force microscopy (AFM), and electrical transport measurements were used as characterization techniques supporting the theoretical predictions of molecular adsorption performed by DFT.

2 Materials and methods

Detailed information on the sample preparation, elemental analysis, characterization by infrared spectroscopy and X-ray diffraction (XRD), DC and AC magnetometry, electrical transport, and HF-ESR measurements is found in the ESI.†

2.1 Deposited samples

For both deposition processes (drop-cast and thermal sublimation) a chemical vapour deposition (CVD) grown monolayer graphene on a Si/SiO$_2$ substrate was used (300 nm thickness of

SiO_2, Si (100), p-doped, 1–10 Ω cm from Graphenea, San Sebastian, Spain). The drop-cast sample was prepared by dissolving the bulk compound **1** or **2** in acetone (99%, Penta, Czech Republic) to make a final solution with a 1 mM concentration. The actual drop-casting was conducted in ambient conditions as 40 μL was drop-cast onto graphene. For the thermal sublimation, we used a home-built high-vacuum sublimation chamber equipped with a quartz crucible heated by a ceramic heater (BACH RC, Seefeld, Germany) with a thermocouple in thermal contact with the heater. The base chamber pressure during the sublimation was 1×10^{-6} mbar. The sublimations for **1** and **2** were performed at 270 and 283, respectively. The bulk powder from the crucible after sublimation was taken for further analysis. Optical images were acquired on a confocal Raman microscope WITec Alpha300 R+ (WITec, Ulm, Germany). All topography images and profiles were obtained with the scanning probe microscope Dimension Icon (Bruker, Billerica, USA) in tapping mode. X-ray photoelectron (XPS) measurements were carried out with Kratos Axis Supra (Kratos Analytical, Manchester, United Kingdom).

2.2 Computational details

The zero-field splitting (ZFS) terms were computed using Gaussian-basis DFT in the ORCA 4.2.1 and 5.0 electronic structure packages,[57,58] using the state average-CASSCF,[59] complemented by NEVPT2.[60,61] The input coordinates for the calculations were obtained from experimentally determined molecular structures refined by Hirshfeld atom refinement[62] incorporated in Olex2 (ver. 1.5).[47] The basis sets for the ZFS calculations were used as follows: def2-SVP for hydrogen and carbon atoms, triple-ζ def2-TZVP for the remaining atoms.[63] The calculation costs were decreased by using the def2/J and def2-TZVP/C auxiliary basis sets[64,65] together with the chain-of-spheres (RIJCOSX)[66,67] approximation to the exact exchange as implemented in ORCA. The active space was defined by seven electrons in five d-orbitals of Co(II) (CAS(7,5)), and all possible multiplets, 10 quartets, and 40 doublets, were involved in the calculations. The ligand field parameters were obtained using the *ab initio* ligand field theory (AILFT) calculations.[68]

BS-DFT calculations in ORCA 5.0 were carried out to estimate the isotropic exchange interaction. Two DFT hybrid functionals, B3LYP[69–71] and PBE0,[72] were selected based on their good performance on previously studied coordination compounds.[73–78] Moreover, the calculations were performed with Ahlrichs triple-ζ basis sets def2-TZVP and also with their relativistic analogs ZORA-def2-TZVP.[63] Furthermore, the non-local density-dependent dispersion correction to DFT was accounted for in two ways, as non-self-consistent (DFT-NL) and as self-consistent (DFT-SCNL) implementation.[79,80]

The quantum theory of atoms in molecules[81] (QT-AIM) calculations were performed using ORCA 4.2.1, employing single-point DFT calculations utilizing the B3LYP functional and bases as described above (def2-TZVP). Then, the wavefunctions were used for the QT-AIM calculations using the Multiwfn program.[82,83] ELF calculations for Co(II) complexes, which visualize electron pairs, were compared to those for diamagnetic Zn(II) analogues, revealing no significant differences.

Molecular adsorption on graphene was calculated using plane-wave DFT performed on the Vienna Ab-Initio Simulation Package (VASP)[84–87] version 5.4.4, which uses a plane-wave basis for the Kohn–Sham orbitals, the Projector Augmented Wave method,[87,88] and pseudopotentials. The exchange–correlation was accounted for by the PBE functional,[89,90] with van der Waals corrections included by the D3 method with Becke–Johnson damping.[91,92] Collinear spin polarization and electric dipole corrections[93,94] were also included. In all calculations, the kinetic energy cut-off for the plane waves was 520 eV, and the cut-off energy of the plane wave representation of the augmentation charges was 644.9 eV. The threshold for electronic self-consistency loops was 10^{-6} eV, and ionic relaxation was performed until residual forces on each ion were below 0.02 eV $Å^{-1}$, unless stated otherwise.

For calculations of the ground-state energy, ionic relaxation of isolated molecules, and ionic relaxation of the molecules on graphene, the reciprocal space was sampled using only one point at the Brillouin zone center (*Γ*-point calculation). For charge density calculations, a *Γ*-centered $2 \times 2 \times 1$ Monkhorst–Pack mesh[95] was used to sample the Brillouin zone of all configurations. The obtained charge densities were used and kept constant in the density of states calculations, where the reciprocal space was sampled with a *Γ*-centered $4 \times 4 \times 1$ Monkhorst–Pack mesh. Reciprocal space integration used Gaussian smearing of *k*-points equal to 0.1 eV. To generate the partial density of states (Fig. 7a), and the planar average of the charge density difference (Fig. 7b, c and ESI† Fig. S41, S42), we used the VASPKIT code.[96] We used the VESTA software[97] to plot Fig. 6a–d, f–i, 7b, c and ESI† Fig. S40–S42.

To model the monolayer graphene substrate, we first performed ionic relaxation of the 10×10 graphene superlattice by plane-wave DFT until the interatomic forces were below 0.001 eV $Å^{-1}$. (1×1 corresponds to a graphene unit cell containing two carbon atoms with an interatomic distance of 1.424 Å.) During the relaxation, the supercell's volume was kept constant, and the ionic positions were relaxed within the graphene's plane. The molecules were modeled taking as a basis their XRD structure. Then, ionic relaxation of the isolated molecules (gas phase) was performed using a parallelepiped unit cell of dimensions $24.67 \times 24.67 \times 30$ $Å^3$ (ESI† Fig. S40). To simulate molecular adsorption on graphene, four different configurations (orientations) of each molecular complex were placed on the 10×10 graphene substrate. A supercell height of 30 Å in the direction perpendicular to the graphene plane (*z* direction), guaranteed at least a 15 Å vacuum above the molecule on the substrate, minimizing the interaction between supercells in the *z* direction. Electric dipole corrections along the *z* direction were applied to reduce this interaction further. The supercell size and shape were kept the same in all calculations.

3 Results and discussion

3.1 Synthesis and structure

Compounds **1** and **2** can be prepared using the previously reported procedure.[41] However, we synthesized both compounds

by *in situ* reaction of 2-amino-6-methylpyridine, salicylaldehyde (or 5- methylsalicylaldehyd for preparation of **2**), $CoCl_2{\cdot}6H_2O$ and triethylamine in methanolic solution (molar ratio 2 : 2 : 1 : 2, Fig. 1). The mixture was refluxed after the addition of all reagents and then filtered. Red-orange crystals suitable for single-crystal XRD were obtained by slow diffusion of Et_2 O into the solution. The purity of both compounds was confirmed by elemental analysis and powder XRD experiments (ESI† Fig. S1). The thermal stability was investigated using thermogravimetric analysis (ESI† Fig. S2 and S3), and it was revealed that compounds **1** and **2** are stable up to 290 and 310 °C, respectively, and with melting temperatures 263–265 and 301 °C, respectively.

Compounds **1** and **2** adopt very similar crystal structures although they are not isostructural. **1** crystallizes in the monoclinic *I*2/*a* space group, whereas **2** in the orthorhombic *Pbcn* space group. The basic crystallographic and refinement data are summarized in the ESI† Table S1. Both crystal structures consist solely of the molecular complex (Fig. 2a and ESI† Fig. S4, S5). In both structures, the cobalt atom sits at a two-fold rotational axis, and thus only half of the complex molecule is symmetrically independent. Two bidentate ligands coordinate the central Co(II) atom, each by one phenolate oxygen atom (d_{Co1-O1} = 1.9527(16) Å and 1.9613(7) Å in **1** and **2**, respectively) and by an imine nitrogen atom (N1 in Fig. 2a, d_{Co1-N1} = 1.9913(18) Å and 1.9923(9) Å in **1** and **2**, respectively). The Co···N distance of the pyridine nitrogen atoms (N2) is longer: 2.6908(19) Å and 2.6951(9) Å in **1** and **2**, respectively, therefore, both **1** and **2** can be formally considered to be tetracoordinate. According to the SHAPE algorithm and continuous shape measurements (CSMs), the shape of the coordination polyhedron corresponds to a distorted tetrahedron (CSMs(T_d): 2.857 and 2.531, respectively), however, distortion from the see-saw geometry is relatively small: (CSMs(C_{2v}): 3.800 and 4.723, respectively, ESI† Table S2). The complex molecules form extensive networks of π–π aromatic stacking interactions organized in supramolecular layers parallel to (00l) planes (in **1**) or chains along the *c*-axis (in **2**, ESI† Fig. S4 and S5).

To investigate the nature of the Co···N interaction we utilized the topological analysis of electron density by QT-AIM. Firstly, we performed single-point DFT calculations using the coordinates of the complex molecules **1** and **2** obtained from XRD experiments. To ensure reliable positions of the hydrogen atoms we applied the Hirshfeld atom refinement for both structures (for details see the ESI† Section S1). Then, we performed topological analysis of the electron density ($\rho(r)$) using Multiwfn software.[82,83] As a result, we did not find any bond critical point (BCP) between the Co1 and N2 atoms, as seen from the Laplacian of electron density ($\nabla^2\rho(r)$, ESI† Fig. S6). This can be attributed to the orientation of the pyridyl moiety, which modulated the topology of $\nabla^2\rho(r)$ between the Co and N atoms, preventing the formation of bond path or BCP (ESI† Fig. S6). Next, we analyzed this interaction using the non-covalent interaction (NCI) method.[98] This method utilizes the analysis of $\rho(r)$ using the reduced density gradient function to distinguish between attractive and repulsive non-covalent interactions by determining the sign of the eigenvalue of the electron density Hessian matrix, defined as λ_2. We visualized the interactions within molecules using VMD software[99] (Fig. 2b). The Co···N interaction was found to be a combination of steric effect (repulsion between the neighboring nitrogen atoms, red color) and attraction between the pair of the Co and N atoms (blue color). To better visualize this interaction, we also computed the electron localization function (ELF), which depicts the probability of finding an electron pair in multielectronic systems.[100,101] Fig. 2c shows that the pyridine electron pair is well localized, pointing towards the more electropositive cobalt atom (ESI† Fig. S6). In summary, despite the absence of BCP, we show that the Co···N interaction exhibits an attractive non-covalent character due to the interaction between the pyridyl electron pair and the cobalt atom. Therefore, we classify this interaction as semi-coordination.[44]

3.2 Magnetic properties and HF-ESR

We employed magnetometry to perform DC magnetic measurements, including temperature- (2–300 K) and field- (0–7 *T* at 2 K)

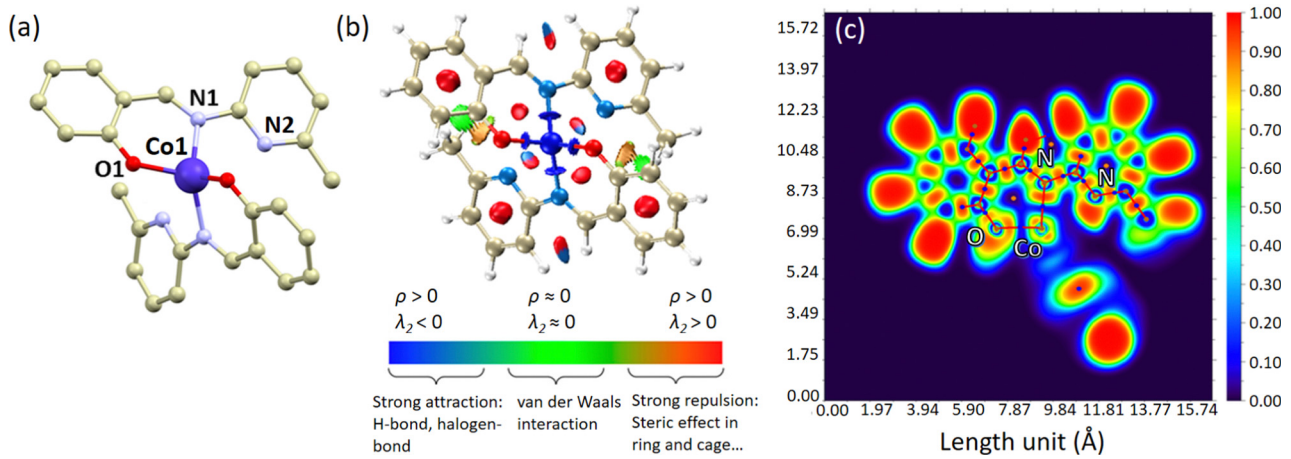

Fig. 2 (a) A perspective view on the structure of the molecular complex in the crystal structure of 1, hydrogen atoms were omitted for clarity. Color code: carbon (light brown), cobalt (dark blue), nitrogen (light blue), and oxygen (red). Selected bond lengths (in Å): 1, d_{Co1-N1} = 1.9970(8), d_{Co1-O1} = 1.9579(7); 2, d_{Co1-N1} = 1.9923(9), d_{Co1-O1} = 1.9613(7). (b) NCI plot calculated for **1**. (c) Visualization of the ELF for 1.

dependence of the magnetic moment (Fig. 3a and ESI† Fig. S27). The crystal structures of **1** and **2** consist of isolated complexes that interact through π–π stacking interactions, which are well-known non-covalent magnetic exchange pathways.[102] To appropriately analyze the magnetic data, we first performed theoretical calculations. We selected dimeric structural fragments (Fig. 3d) and conducted BS-DFT calculations following the procedure of Section 2.2 to estimate the isotropic exchange of the spin Hamiltonian defined as $\hat{H} = -J\hat{S}_1\cdot\hat{S}_2$, with $\hat{S}_1$ and $\hat{S}_2$ corresponding to the spin operator of each molecule in the dimer. The comparison of the energy difference between the high-spin (HS, $S_{1\uparrow}\cdots S_{2\uparrow}$) and broken-symmetry spin states (BS, $S_{1\uparrow}\cdots S_{2\downarrow}$), $\Delta = \varepsilon_{BS} - \varepsilon_{HS}$, was utilized to calculate J according to the formulas of Ruiz[103] and Yamaguchi:[104]

$$J^R = \frac{2\Delta}{(S_1+S_2)(S_1+S_2+1)}, \quad J^Y = \frac{2\Delta}{\langle S^2\rangle_{HS} - \langle S^2\rangle_{BS}}. \quad (1)$$

All approaches predicted a weak antiferromagnetic coupling within the dimer for compounds **1** and **2** using all tested functionals and bases (see the ESI,† Tables S8 and S9); for example, using the functional B3LYP + NL we find $J^Y = -0.247$ cm^{-1} and -0.268 cm^{-1} for **1** and **2**, respectively. A slightly stronger antiferromagnetic exchange was predicted for **2**, which is consistent with its shorter C···C and C···N distances between the π–π stacked ligands of the neighboring molecules compared to those in compound **1**. The magnetic exchange interaction between neighboring molecules is expected to be weak due to the relatively large Co···Co distances being 5.94479(9) and 5.82467(7) Å in compounds **1** and **2**, respectively.

Since the magnetic measurements for both compounds were very similar, we provided a more detailed description of the properties of **1**. The effective magnetic moment μ_{eff}/μ_B measured for **1**, where μ_B is the Bohr magneton, adopts a value of 4.3 at room temperature, which is consistent with a large contribution of SOC. Thus, the Landé g-factor (g_{iso} = 2.20) is larger than that of the free electron (g = 2.0023). The μ_{eff}/μ_B values stayed approximately constant down to 30 K, where we observed a drop starting from 4.1 to 3.7 at 2 K suggesting the presence of intermolecular magnetic exchange interactions or ZFS. Since we did not observe maxima in the susceptibility curve ($\chi = f(T)$), we may conclude that the intermolecular magnetic interactions among molecules are weak. Nevertheless, we were unable to fit the magnetic data in the absence of exchange coupling, and due to this fact as well as taking into account the results of BS-DFT calculations, we applied a spin Hamiltonian including axial (D) and rhombic (E) single-ion ZFS

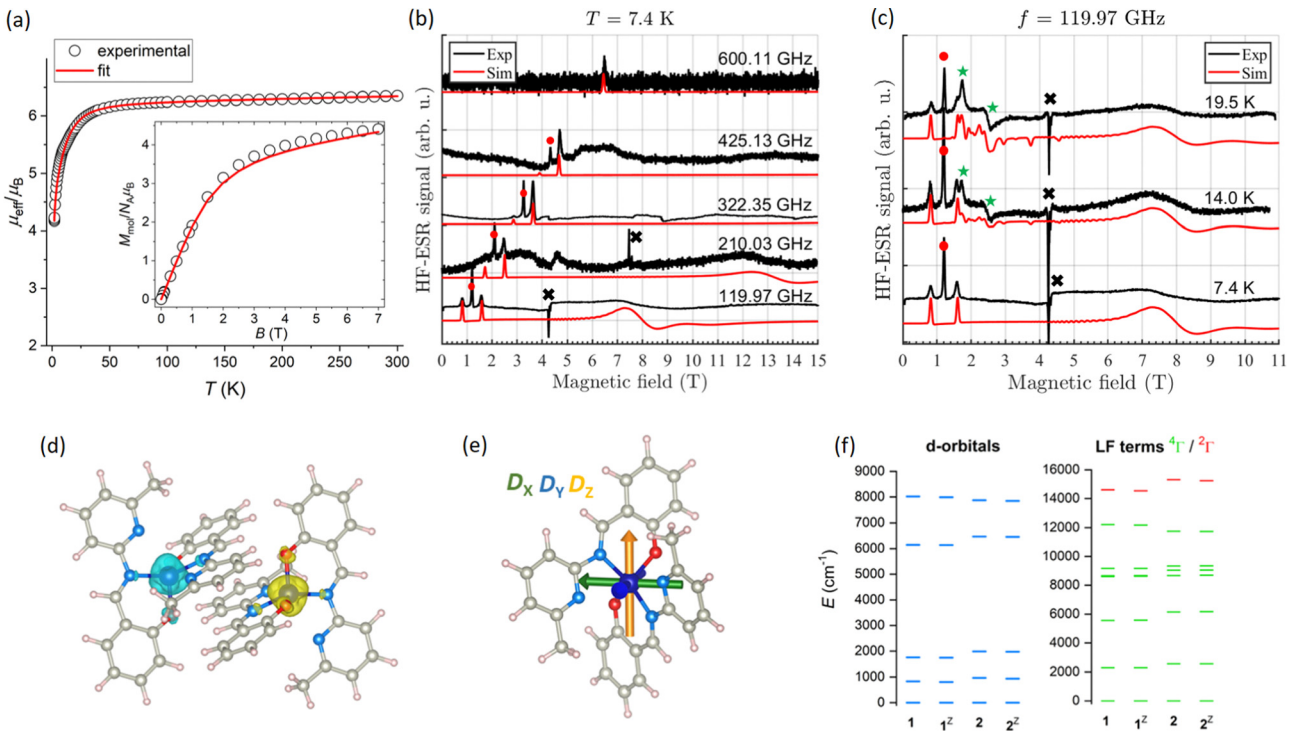

Fig. 3 (a) Temperature dependence of μ_{eff}/μ_B acquired for 1 in the range from 2 K to 300 K with an external magnetic field 0.1 T, and the isothermal magnetization data measured at 2 K shown in the inset. The empty circles represent experimental data, while the red lines represent fittings to eqn (2)–(4). (b) Frequency dependence of the HF-ESR spectra of compound **1** at 7.4 K. (c) Temperature dependence of the HF-ESR spectra of compound 1 at 119.97 GHz. The parameters in the simulated spectra (with offset for more clarity) were $D = -20$ cm^{-1}, g_x = 2.20, g_y = 2.15, g_z = 2.40, E/D = 0.122, and $J = -0.3$ cm^{-1}. Green stars correspond to thermally-activated transitions ascribed to the excited S = 1/2 doublet, black crosses indicate an ESR signal from an impurity in the sample holder's mirror, and red dots indicate a spurious signal not considered in the simulation. (d) The outcome of the BS-DFT calculations for 1 with visualization of the spin density isosurface. (e) Visualization of the D-tensor axes overlayed over the molecular structure of 1. (f) AILFT-calculated d-orbital splitting (left) and ligand field terms (right).

terms and exchange coupling for the supramolecular dimer:

$$\hat{H} = -J(\hat{S}_1 \cdot \hat{S}_2) + D\left(\hat{S}_z^2 - \frac{S^2}{3}\right) + E\left(\hat{S}_x^2 - \hat{S}_y^2\right) + \mu_B B g \hat{S}_a, \quad (2)$$

together with the Zeeman term defined in the direction of the magnetic field as $B_a = B(\sin\theta\cos\phi, \sin\theta\sin\phi, \cos\theta)$, where θ and ϕ are the polar and azimuthal angles of the field. The molar magnetization in the a-direction of the magnetic field was numerically calculated from the partition function, Z, built from the energy levels of the spin Hamiltonian as follows:

$$M_a = N_A k_B T \frac{\mathrm{d}\ln Z}{\mathrm{d}B_a}, \quad (3)$$

where k_B and N_A are the Boltzmann and Avogadro constants, respectively. Then, the averaged molar magnetization of the powder sample was calculated as the orientational average:

$$M_{mol} = \frac{1}{4\pi}\int_0^{2\pi}\int_0^{\pi} M_a \sin\theta \mathrm{d}\theta\mathrm{d}\phi. \quad (4)$$

The experimental magnetic data were fitted using EasySpin,[105] analyzing both temperature- and field-dependent measurements simultaneously. The best fit was obtained with the following sets of parameters: for **1**, $J = -0.19$ cm^{-1}, $g_{iso} = 2.272$, $D = -15.3$ cm^{-1} and $E/D = 0.012$; for **2**, $J = -0.27$ cm^{-1}, $g_{iso} = 2.213$, $D = -17.5$ cm^{-1} and $E/D = 0.044$ (Fig. 3a and ESI† Fig. S27). This confirmed the presence of a relatively large and axial magnetic anisotropy.

ZFS was studied theoretically using the procedure outlined in Section 2.2, using ORCA 5.0. The calculations indicate that the ^{4}F atomic term is split into seven ligand field multiplets as expected due to the low symmetry of the coordination polyhedron in **1** and **2**. Additionally, the energy of the first excited state is above 1000 cm^{-1}, making the spin Hamiltonian formalism suitable for analyzing magnetic data.[106] The splitting of the d-orbitals reflects the distorted tetrahedral geometry with the lowest $d_{x^2-y^2}$ orbital. The configuration of the d-orbitals is for both complexes as follows: $d_{x^2-y^2}{}^2$, $d_{z^2}{}^2$, $d_{xy}{}^1$, $d_{xz}{}^1$, $d_{yz}{}^1$ (ESI† Fig. S21 and S22). In this configuration, the energy of the first excitation between the d-orbitals with the same $|m_l|$ value ($d_{x^2-y^2}{}^2 \rightarrow d_{xy}{}^1$, $|m_l| = 2$) is smaller than the first excitation with $\Delta|m_l| = 1$ ($d_{z^2}{}^2 \rightarrow d_{xz}{}^1$). This indicates a relatively large and axial magnetic anisotropy.[23] CASSCF-NEVPT2 calculations of the ZFS parameters confirmed this assumption: $D = -25.3$ cm^{-1} and $E/D = 0.084$ for **1**; $D = -28.3$ cm^{-1} and $E/D = 0.107$ for **2** (ESI† Tables S10 and S11). The obtained ZFS parameters were markedly different from those obtained by magnetometry. Therefore, we investigated if the used basis sets can help to diminish the difference between the calculated and experimentally derived ZFS parameters. We included relativistic effects by introducing relativistic analogs of Ahlrichs double- and triple-ζ basis sets (ZORA-def2-SVP for hydrogen and carbon atoms). The calculated D values were slightly lower than those resulting from non-relativistic calculations, but their absolute values are still significantly larger than those derived from magnetometry (ESI† Tables S10 and S11).

We investigated the impact of the pyridine nitrogen atoms on the electronic structure and magnetic anisotropy of compounds **1** and **2** by replacing the 6-methyl-pyridine groups with phenyl rings. Using DFT calculations (B3LYP and def2-SVP in ORCA 5.0) we optimized the positions of these new groups while keeping the positions of other atoms fixed, resulting in the **1′** and **2′** input structures. This method allowed us to maintain the ligand field strength and symmetry from the regular donor atoms ($\{NO\}_2$) while eliminating any influence of the pyridine nitrogen atoms. The CASSCF-NEVPT2 calculations for **1** and **2** yielded very similar ligand field term structures as in **1** and **2**. However, the energy of the lowest quartet was found to be lower in **1** and **2** compared to **1** and **2** (ESI† Fig. S23–S25). The resulting ZFS parameters are different from those obtained for **1** and **2**; the $|D|$ values were found to be larger (-40.3 cm^{-1} for **1** and -38.1 cm^{-1} for **2**) while the E/D values were significantly lower ($E/D = 0.055$ in **1**, 0.039 in **2**).

Thus, the anisotropy of **1** and **2** is larger and less rhombic than calculated for **1** and **2**. The larger $|D|$ values can be explained by the d-orbital splitting. Despite having the same splitting pattern and similar orbital energies as **1** and **2**, the observed changes in **1** and **2** are most pronounced for the d_{xy} orbital, which experiences the greatest decrease in energy (ESI† Fig. S25). This aligns with the orientation of this orbital in relation to the position of the pyridyl rings. In **1** and **2**, the pyridyl nitrogen atoms point towards the lobes of the d_{xy} orbital (ESI† Fig. S25). However, in **1** and **2**, the orientation of the orbital remains unchanged even without the pyridyl nitrogen atoms. It is worth noting that the decrease of the d_{xy} energy is larger in **2** than in **1** which correlates with the shorter Co$\cdots$N distance (and thus larger destabilization of d_{xy}) in **2** (2.6592(9) Å) than in **1** (2.6901(11) Å). As a result, the lower energy of the d_{xy} orbital leads to a smaller $d_{x^2-y^2}{}^2 \rightarrow d_{xy}{}^1$ excitation, resulting in larger $|D|$ values. In summary, the CASSCF-NEVPT2 calculations revealed that while the interaction between the Co(II) atom and pyridyl nitrogen atoms does not induce significant changes in the overall ligand field, the interaction between the d_{xy} orbital and lone pairs of the nitrogen atoms produce smaller $|D|$ values in complexes with the Co$\cdots$N interactions.

The magnetization blocking barriers in **1** and **2** were calculated using the SINGLE_ANISO module[107] incorporated in ORCA 5.0.[58] The results strongly indicate that quantum tunneling is the dominant relaxation process since the matrix element of the transversal magnetic moment between the ground states with opposite magnetizations is greater than 0.1 (0.23 for **1**, 0.18 for **2**, ESI† Fig. S26). Therefore, it is expected that **1** and **2** will behave as field-induced SIMs. Notably, changing the basis from non-relativistic to relativistic (def2-TZVP *vs.* ZORA-def2-TZVP) did not affect the matrix elements of any of the calculated magnetic moments (ESI† Fig. S26).

Further analysis of the magnetic properties of **1** was performed by HF-ESR. Although measurements were taken on compounds **1** and **2** both in powder form and deposited on graphene, only the powder spectra of **1** showed satisfactory results. HF-ESR measurements on the deposited compounds on graphene did not show a clear signal due to the low

deposited amounts, as evidenced in the ESI† Fig. S30 for compound **1**. Fig. 3b and c show the HF-ESR powder spectra of **1** at different frequencies and temperatures, respectively. (HF-ESR spectra at other frequencies are shown in the ESI† Fig. S28.) From the temperature-dependent spectra, we observed strong thermally-activated transitions ascribed to the $S = 1/2$ doublet, indicated by green stars in the spectra, confirming that the ground state has spin 3/2, and thus D is negative. Nevertheless, transitions between the ground-state $S = 3/2$ and the excited state $S = 1/2$ were not observed in the energy range accessible in our experiments. Therefore, we set a bound for the ZFS such that the mentioned transition does not appear in the simulated spectrum, being equal to $|D| > 600$ GHz = 20 cm^{-1}. Simulations with the parameters $g_x = 2.20$, $g_y = 2.15$, $g_z = 2.40$, $D = -20$ cm^{-1}, $E/D = 0.122$, and an exchange term $J = -0.3$ cm^{-1} reproduce most of the spectral features successfully and suggest intermolecular antiferromagnetic coupling, in agreement with BS-DFT calculations ($J^{Y} = -0.247$ cm^{-1}, B3LYP-NL method), and similar to the one found by DC magnetometry ($J = -0.19$ cm^{-1}). The ZFS parameters g-factors are in agreement with the ones calculated for **1** in bulk configuration by CASSCF-NEVPT2, as shown in Section 3.4 and Table 3. Although weak, the exchange coupling has a noticeable effect on the HF-ESR spectra, since it is responsible for the emergence of a second peak in the low magnetic field region (the first two peaks in the simulated spectra of Fig. 3b). The separation between those peaks indicates the strength of the exchange coupling, such that at $J = 0$ there is only one peak in the low magnetic field region. Of the spectral features not captured in the simulation, the ones indicated by black crosses correspond to a signal coming from the mirror in the sample holder, while for the ones indicated by red dots, we do not have a conclusive explanation. From the simulations, we can infer that they do not come from plausible values of the spin Hamiltonian parameters for compound **1**.

To probe the slow relaxation of magnetization behavior in **1** and **2**, the AC susceptibility was measured at low temperatures (see the ESI† Section S7 for a detailed experimental description of AC susceptibility measurements and data analysis). At 2 K, a static magnetic field (B_{DC}) scan revealed the absence of an out-of-phase signal χ'' at $B_{DC} = 0$ T for both compounds (ESI† Tables S13, S21 and Fig. S31, S35), which is a consequence of fast relaxation of magnetization resulting from the quantum tunneling (QT) effect induced by hyperfine interactions with nuclear spins. However, the applied B_{DC} field suppressed the tunneling, allowing us to map the AC susceptibility and find the optimal B_{DC} field for further temperature-dependent dynamic magnetic investigations. The frequency-dependent in-phase χ' and out-of-phase χ'' components of the AC susceptibility were satisfactorily fitted to the extended one-set Debye model (ESI† eqn. (S1), (S2), Tables S13, S21 and Fig. S31, S35), by which the isothermal χ_T and adiabatic χ_S susceptibilities along with the relaxation time τ (Fig. 4a) and its distribution parameter α were determined at given B_{DC} fields.

The global relaxation rate τ^{-1} is usually described by Orbach, Raman, direct, and QT relaxation processes as follows:

$$\frac{1}{\tau} = \frac{1}{\tau_{Orbach}} + \frac{1}{\tau_{Raman}} + \frac{1}{\tau_{direct}} + \frac{1}{\tau_{QT}} = \frac{1}{y_0}\exp\left(-\frac{U}{k_B T}\right) + d\left(\frac{1+eH^2}{1+fH^2}\right)T^n + aH^m T + \frac{b_1}{1+b_2H^2}. \quad (5)$$

At very low temperatures (*i.e.* at 2 K), the Raman, direct or QT terms of eqn (5) usually participate in the relaxation of magnetization; therefore, the τ *vs.* B_{DC} dependencies for both compounds were analyzed with the respective combinations of direct & QT or direct & Raman mechanisms. No combination of these mechanisms was appropriate for the τ *vs.* B_{DC} analysis of **1** (ESI† Fig. S31d and Table S16), while a combination of direct & Raman processes gave satisfactory results in the low field region 0–0.1 T of **2** (ESI† Fig. S35d and Table S24).

The longest relaxation times were observed at $B_{DC} = 0.06$ T for **1** and $B_{DC} = 0.09$ T for **2** (Fig. 4a) and these static fields were used for further temperature-dependent dynamic magnetic studies. Additionally, slightly higher static fields ($B_{DC} = 0.09$ T for **1** and $B_{DC} = 0.125$ T for **2**) were used to record the same acquisition of dynamic magnetic measurements upon the change of temperature, enabling a comprehensive analysis of the slow relaxation of magnetization in both investigated SIMs

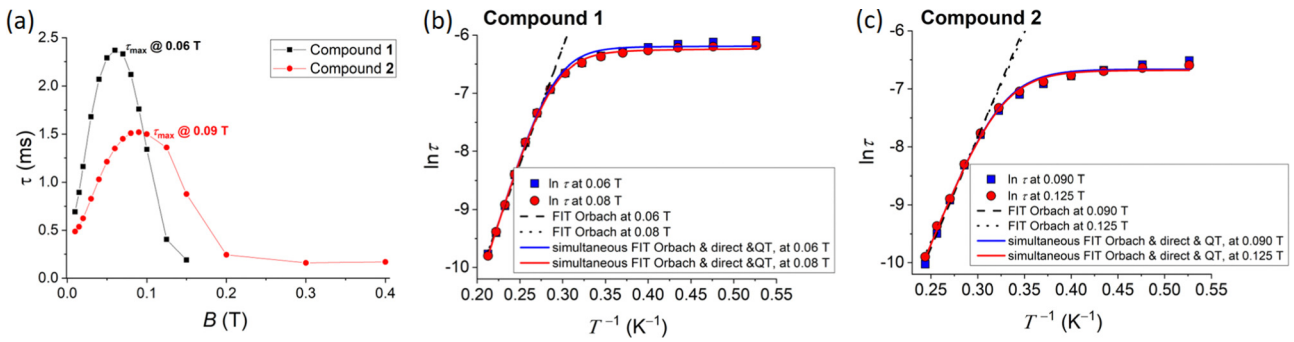

Fig. 4 (a) τ *vs.* B_{DC} dependencies for compounds **1** and **2**. (b) and (c) $\ln\tau$ *vs.* $1/T$ plots for compounds **1** and **2**, respectively, obtained from AC susceptibility measurements recorded at two different DC magnetic fields. The blue and red solid lines result from simultaneous fits of two $\ln\tau$ *vs.* $1/T$ dependencies at two different DC magnetic fields for each compound.

(*vide infra*). Frequency-dependent in-phase (χ') and out-of-phase (χ'') components of the magnetic susceptibility measured as a function of the frequency of an alternating magnetic field, B_{AC}, for a set of temperatures (1.9–4.9 K for **1** and 1.9–4.1 K for **2**; ESI† Fig. S32, S33, S36, S37 and Tables S14, S15, S22, S23) suggest a single relaxation channel. The out-of-phase components χ'' for **1** and **2** show the maximum shift from 69 Hz (at 1.9 K and 0.06 *T*, $\tau \approx 2.3$ ms) and from 106 Hz (at 1.9 K and 0.09 *T*, $\tau \approx 1.5$ ms), respectively, towards higher frequencies upon a temperature increase (ESI† Tables S14, S15, S22 and S23). This indicates a typical feature of SMMs – the maxima of χ'' are frequency and temperature dependent, and the relaxation time τ shortens as the temperature increases. The temperature-dependent AC susceptibility measurements were fitted using an extended one-set Debye model (ESI† eqn (S1) and (S2)), which enabled us to obtain the relaxation time τ at the corresponding temperatures and static magnetic fields. The analysis of temperature dependencies $\ln\tau$ *vs.* $1/T$ at a given B_{DC} was carried out with respect to various combinations of relaxation processes involved in the following relaxation equation:

$$\frac{1}{\tau} = \frac{1}{\tau_{Orbach}} + \frac{1}{\tau_{Raman}} + \frac{1}{\tau_{direct}} + \frac{1}{\tau_{QT}} = \frac{1}{y_0}\exp\left(-\frac{U}{k_B T}\right) + CT^n + aH^m T + \frac{1}{\tau_{QT}}, \quad (6)$$

where the corresponding terms represent Orbach, Raman, direct, and QT relaxation mechanisms, respectively. The most successful fits with the reliable values of relaxation parameters involve the combination of Orbach, direct, and QT mechanisms for **1** (ESI† Tables S17 and S18) and Orbach, direct, and Raman mechanisms for **2** (ESI† Tables S25 and S26). A more comprehensive analysis was focused on the simultaneous fitting of $\ln\tau$ *vs.* $1/T$ functions at two static B_{DC} fields. Thus, two $\ln\tau$ *vs.* $1/T$ dependencies recorded at 0.06 and 0.08 *T* for **1** and at 0.09 and 0.125 *T* for **2** were simultaneously analyzed using combinations of various relaxation mechanisms. The most accurate fits involve the combination of Orbach, direct, and QT processes for each compound (Fig. 4b, c and ESI† Tables S19, S27). The Orbach energy barriers (U_{eff}) and relaxation time at infinite temperature (τ_0) are comparable to the previously reported tetracoordinated Co(II) field-induced SIMs with a similar degree of tetrahedral distortion and magnetic anisotropy (see the ESI† Table S28 for a comparison with similar compounds in other studies). Furthermore, the obtained relaxation parameters suggest that the presence of methyl substituents introduced on the tridentate Schiff base ligand accelerates the slow relaxation of magnetization governed *via* QT and Orbach relaxation, while the direct relaxation seems to be unaffected by such subtle structural variation. Table 1 summarizes the main results from the AC susceptibility analysis.

Table 1 Relaxation parameters for the reported compounds. Fits considering only the Orbach relaxation process were obtained by fitting the high-temperature parts of $\ln\tau$ *vs.* $1/T$ at the corresponding B_{DC} fields. Comprehensive fitting analysis of $\ln\tau$ *vs.* $1/T$ involves simultaneous fittings at two B_{DC} fields

Compound, Model	U (K)	τ_0 (ns)	τ_{QTM} (ms)	a (T^m K s)$^{-1}$ / m
1, Orbach[a] at 0.06 *T*	40	12	—	— / —
1, Orbach[a] at 0.08 *T*	40	11	—	— / —
1, Orbach & direct & QT[b]	48.2	2.0	2	4×10^4 / 4 (fixed)
2, Orbach[c] at 0.09 *T*	38	4	—	— / —
2, Orbach[c] at 0.125 *T*	36	8	—	— / —
2, Orbach & direct & QT[d]	41	2.2	1.3	4×10^4 / 4 (fixed)

[a] For data in the range 3.5–4.7 K. [b] At 0.06 *T* and 0.08 *T*. [c] For data in the range 3.3–4.1 K. [d] At 0.09 *T* and 0.125 *T*.

3.3 Deposition and charge transfer

Depositions on CVD graphene on Si/SiO_2 by drop-cast and thermal sublimation were performed to test the stability of both compounds. Optical images of deposited compounds **1** and **2** can be seen in Fig. 5a and Fig. S7, S14 (ESI†). The topography of both samples was investigated by AFM (Fig. 5(b, c) and Fig. S7, S14, ESI†), revealing that drop-cast depositions led to the formation of crystals a few micrometers high, while thermal sublimation resulted in islands with heights up to 150 nm for **1** (Fig. 5c), and 50 nm for **2** (ESI† Fig. S13). Raman spectroscopy and XPS confirmed that the chemical identity of the molecules was preserved upon the deposition by both drop-cast and thermal sublimation, a detailed comparison of XPS and Raman spectroscopy on the deposited samples with a bulk reference is found in the ESI† Sections S3 and S4. Raman spectra revealed a consistent shift of graphene's 2D peak ($\sim$2690 cm^{-1}) towards lower energy values after the deposition of both compounds (Fig. 5d and ESI† Fig. S8, S15), which, considering that graphene was initially p-doped due to the contact with impurities under ambient conditions, suggests n-doping of graphene arising from electron transfer from the compounds.[108,109] n-Doping was further confirmed in transport measurements on samples deposited on graphene field-effect transistors (GFETs). To assess the charge transfer characteristics, **1** and **2** were drop-cast onto GFETs, following the procedure in the ESI† Section S8. The conductance through the devices was monitored as the gate voltage was varied from zero to 100 V, as shown in Fig. 5e and Fig. S39 (ESI†). As fabricated, the charge neutrality point (conductivity minimum) of the devices was approximately 95 V. With **2** deposited, the charge neutrality point shifted by -23 V, indicating significant electron transfer to the graphene. Charge transfer was less apparent in devices coated with **1** (ESI† Fig. S39). The charge transfer effect may be much weaker with **1**, or a lower coverage of the devices may have muted the effect.

3.4 Theoretical calculations of molecular deposition and their magnetic properties

To simulate the molecular adsorption on graphene, we followed the procedure described in Section 2.2. For each molecular complex, we considered four different molecule orientations relative to the graphene substrate, based on the

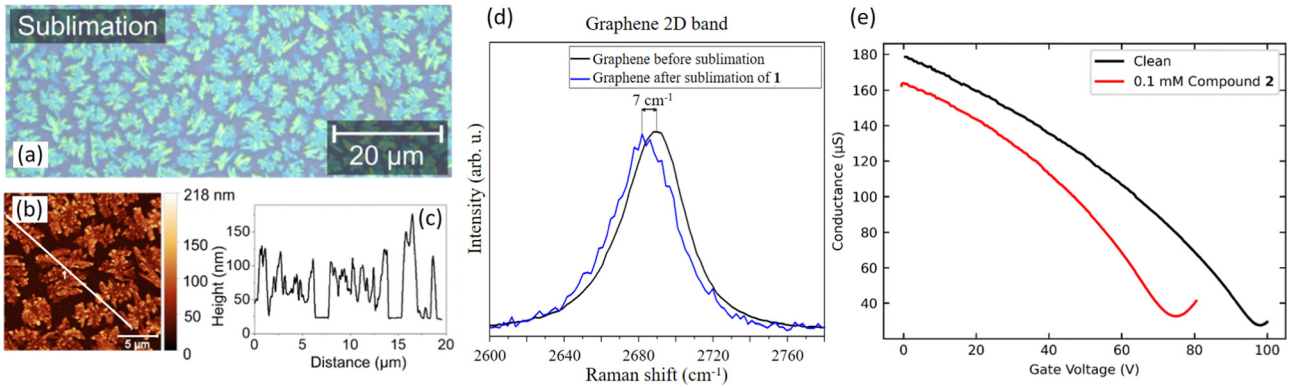

Fig. 5 (a) Optical image of deposited compound **1** (in green) on CVD graphene (dark blue) by thermal sublimation. (b) AFM image of deposited compound **1** on CVD graphene by sublimation. (c) The height profile along the white line indicated in the AFM image. (d) Raman spectra of the 2D band of graphene before and after sublimation of compound **1**. The wavelength of the laser source was 532 nm. (e) Gate-dependent conductivity through GFETs before and after deposition of compound **2** by drop-casting.

possible enhancement of hydrogen–carbon and carbon–carbon interactions between the molecule and substrate, as shown in Fig. 6a–d and f–i. Then, the molecules in each configuration were placed on top of the substrate, such that the ground state energy of the whole system was calculated, but without performing ionic relaxation. By varying the relative distance between the molecule and substrate, we generated the energy profiles in Fig. 6e and j for each configuration. The presence of energy minima in the profiles confirms that there is an attractive interaction between the molecule and substrate, which allows estimating the equilibrium distance of each system. We performed a third-degree polynomial fit to each curve to estimate the equilibrium distances, d_{eq}, and the results are found in Table 2. The distance between molecule and substrate was defined as the distance between the closest H atom to the graphene plane. We found that the equilibrium distances are in the range 2.50–2.72 Å for **1**, and 2.24–2.65 Å for **2**.

To determine the binding energies and equilibrium geometries of the molecules on graphene, we positioned the molecule in each configuration at the equilibrium distance and performed ionic relaxation of all ions (molecule and substrate) by plane-wave DFT. After obtaining the relaxed structure, we took the resulting molecule and substrate separately and computed a DFT self-consistent cycle for each of them to obtain the total energy of the individual systems. In this procedure, the binding energies were computed as

$$E_{bin} = E_{mol+subs} - E_{mol} - E_{subs}, \quad (7)$$

where $E_{mol+subs}$, E_{mol}, and E_{subs} are the total energies of the molecule + substrate, isolated molecule, and isolated substrate, respectively. Table 2 shows the binding energies and changes in the relative distances between the Co center and its nearest neighbors. We found that both compounds have comparable equilibrium distances and binding energies, with **Conf. 4**

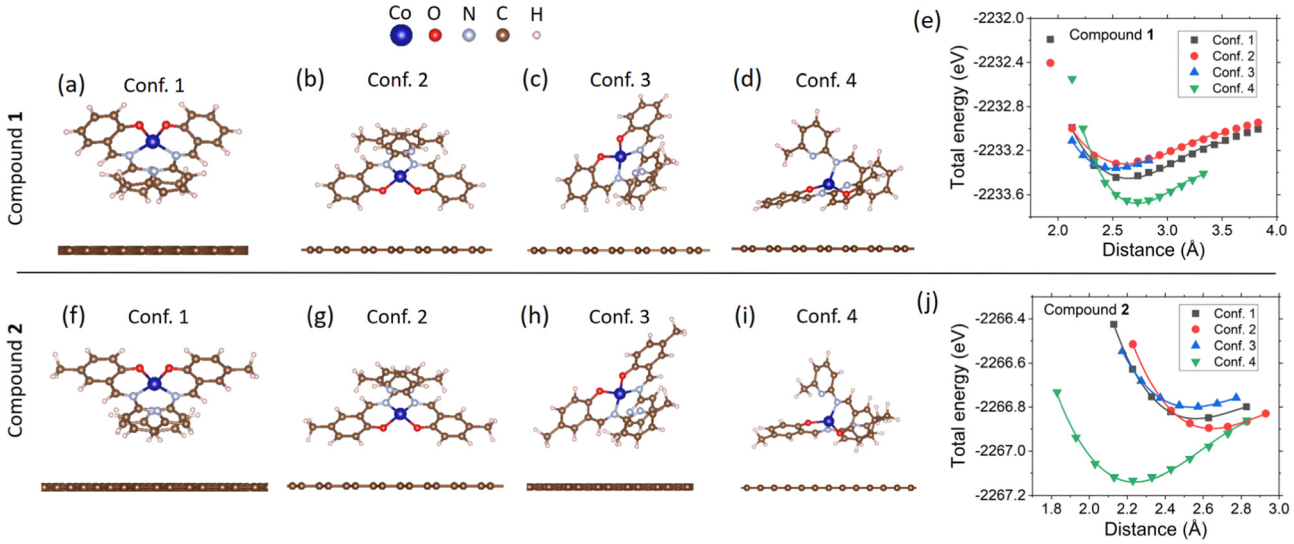

Fig. 6 Model systems used for plane-wave DFT calculations. (a)–(d) Configurations **1** to **4** of compound **1** with different orientations relative to the substrate. (e) Energy profile of compound **1** on graphene in all configurations, as a function of the distance to the graphene plane. The distance is defined as the distance between the closest hydrogen atom of the molecule to the substrate. Continuous lines represent fittings to a third-degree polynomial. (f)–(i) Configurations 1 to 4 of compound **2**. (e) Energy profile of compound **2** on graphene in all configurations.

Table 2 Equilibrium distances (d_{eq}) of the molecules on graphene in each configuration as determined from the energy profiles of Fig. 6e and j, binding energies (E_{bin}), distances between the Co center and its neighbors (d_{Co1-X}), HOMO–LUMO gap ($\Delta E_{HOMO-LUMO}$), electron transfer from molecule to substrate (Δq, in units of number of electrons), and total magnetization of each configuration of molecule on the surface (μ), as calculated by plane-wave DFT

System	d_{eq} (Å)	E_{bin} (eV)	d_{Co1-N1} (Å)	d_{Co1-N2} (Å)	d_{Co1-O1} (Å)	$\Delta E_{HOMO-LUMO}$ (eV)	Δq (e^-)	μ (μ_B)
1 XRD (exp.)	—	—	1.991	2.691	1.953	0.64	—	3.000
1 Isolated, DFT relax.	—	—	1.954	2.860	1.918	0.85	—	3.000
1 Conf. 1	2.61	−0.83	1.955	2.856	1.917	0.76	0.065	3.078
1 Conf. 2	2.59	−0.70	1.957	2.858	1.917	0.73	0.003	3.006
1 Conf. 3	2.50	−0.73	1.955	2.816	1.917	0.76	0.056	3.075
1 Conf. 4	2.72	−1.08	1.955	2.811	1.919	0.74	0.016	3.020
2 XRD (exp.)	—	—	1.992	2.695	1.961	0.65	—	3.000
2 Isolated, DFT relax.	—	—	1.954	2.776	1.918	0.84	—	3.000
2 Conf. 1	2.56	−0.90	1.955	2.768	1.921	0.75	0.084	3.099
2 Conf. 2	2.65	−0.92	1.955	2.782	1.917	0.74	0.014	3.020
2 Conf. 3	2.54	−0.80	1.954	2.772	1.917	0.76	0.078	3.095
2 Conf. 4	2.24	−1.15	1.957	2.768	1.921	0.73	0.033	3.045

having the highest binding energy (in absolute value) in both complexes. Nevertheless, we cannot conclude at this point that this is the preferred molecular orientation on graphene since the binding energies of the other configurations are comparable in value. The relatively low binding energy ($|E_{bin}| \lessapprox 1.2$ eV per molecule) of the studied configurations suggests that the binding mechanism is through van der Waals forces and could explain the tendency of the molecules to form clusters on graphene due to the low interaction with the substrate, as observed by optical microscopy and AFM images (Fig. 5a, b and ESI† Fig. S7, S14). With the aim of comparing the deposited molecules with the bulk structure (the initial experimental configuration found by XRD) and the isolated molecule relaxed by plane-wave DFT without substrate, in Table 2 we include the distances from the Co center to the immediate coordination atoms (d_{Co1-N1}, d_{Co1-O1}), and the pyridyl nitrogen (d_{Co1-N2}). The highest deviation in the relative distances was found between the initial XRD structure and the isolated, DFT-relaxed molecule; the distances from the Co center to the coordination ions N1 and O1 were slightly reduced in both compounds, while the distance to the pyridyl nitrogen N2 increased by 0.169 Å and 0.081 Å for **1** and **2**, respectively. These changes are expected since the effects of neighboring molecules in the crystal structure are present in the bulk compound, and subjecting the molecule to external forces that are absent in the isolated configuration. After adsorption, DFT calculations show only small deviations from the isolated configuration, consistent with the weak van der Waals interaction between molecule and substrate.

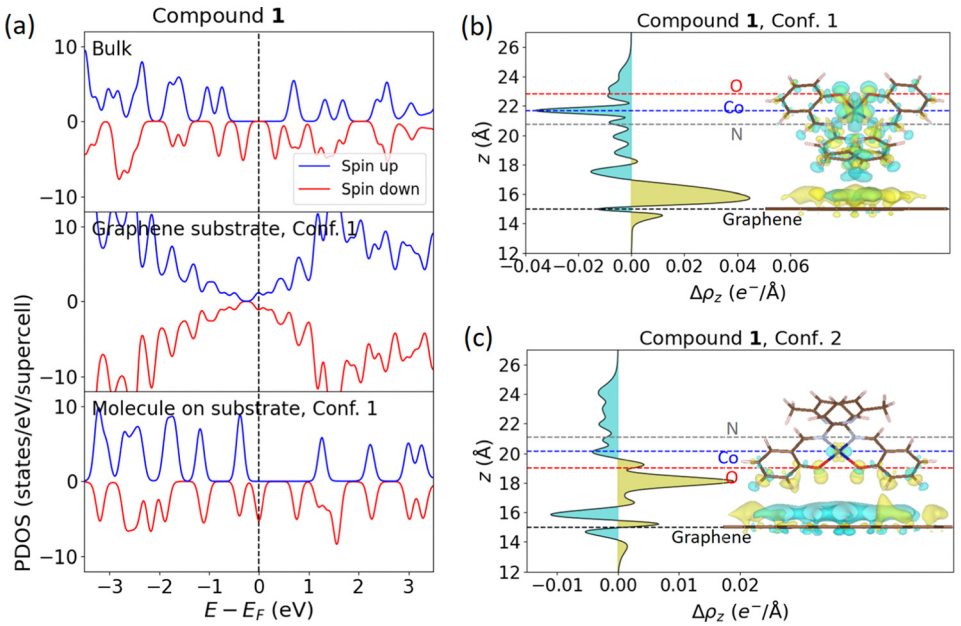

Fig. 7 (a) Comparison between the DOS of **1** in the bulk (XRD) structure, the PDOS of graphene in **Conf. 1**, and the PDOS of compound **1** on graphene in **Conf. 1**. The dashed vertical line indicates the Fermi energy. (b) and (c) Planar average of the charge density difference of compound **1** in **Conf. 1** and **2**, respectively. Superimposed on them are isosurface plots of the charge density difference, $\Delta\rho$. The isosurface level is 1.01×10^{-3} e^- Å^{-3} yellow and cyan colors represent the accumulation and depletion of electrons, respectively. Dashed lines indicate the location of graphene, Co atom, and coordination N and O atoms.

We now study the changes in the highest occupied and lowest unoccupied molecular orbitals (HOMO and LUMO, respectively) after deposition. In the bulk structure and isolated, DFT-relaxed molecules, the HOMO–LUMO gap ($\Delta E_{\mathrm{HOMO-LUMO}}$) was obtained from the total density of states (DOS), while in the molecule + substrate system, it was obtained from the partial density of states (PDOS), selecting only the molecule's electronic orbitals. Fig. 7a shows a comparison between the DOS of **1** in the bulk structure and the PDOS of graphene and molecule in **Conf. 1** after deposition (ESI† Fig. S43 and S43 show the PDOS of all systems). The results of the HOMO–LUMO gap, shown in Table 2, indicate a noticeable change in the quantity in all considered systems. In particular, graphene affects the HOMO–LUMO gap of the deposited molecules, decreasing it by around 0.1 eV, considering that the initial system for plane-wave DFT calculations of molecular adsorption was the isolated, DFT relaxed molecules, which have a HOMO–LUMO gap of 0.85 eV and 0.84 eV for **1** and **2**, respectively. In Fig. 7a, we observe a depopulation of the molecules HOMO after deposition, leading to a population of graphene conduction bands and consequently, to n-doping of graphene. This is consistent in all studied configurations of both molecular complexes, as shown in the ESI† Fig. S43 and S44. Transport measurements (Fig. 5e and Fig. S39, ESI†) and Raman spectroscopy (Fig. 5d and ESI† Fig. S8, S15) confirmed electron transfer from the molecule to graphene, leading to n-doping of graphene.

To obtain a better understanding of the electron transfer behavior between the molecule and substrate, we performed Bader charge analysis[81] as implemented by Henkelman *et al.*[110,111] The results, shown in Table 2 for each configuration, indicate a consistent electron transfer from molecule to substrate, in agreement with the results from DOS analysis. Although such electron transfer is below 0.1 e^-, it is observed that it has a direct effect in increasing the total magnetization of the system, compared to a value of 3.00 μ_B for isolated molecules, corresponding to three unpaired electrons of Co(II). The increase in magnetization is consistent with electron transfer from the molecule's HOMO to graphene, which has spin-down polarization as observed in Fig. 7a, and consequently, increasing the spin polarization of the molecules charge density (difference between spin up and spin down charge densities).

To analyze further the charge transfer behavior, we computed the charge density difference, defined as

$$\Delta\rho = \rho_{\mathrm{mol+subs}} - \rho_{\mathrm{mol}} - \rho_{\mathrm{subs}}, \quad (8)$$

where $\rho_{\mathrm{mol+subs}}$, ρ_{mol}, and ρ_{subs} are the charge densities of the molecule + substrate, isolated molecule, and isolated substrate, respectively. Fig. 7b and c show the isosurface plots and planar average of the charge density difference ($\Delta\rho_z$, with $\Delta\rho$ averaged over the *xy* plane) of compound **1** in **Confs. 1 and 2** (plots of all configurations are found in the ESI,† Fig. S41 and S42). For both compounds, **Confs. 1 and 3** show a clear charge accumulation near graphene, while in **Confs. 2 and 4** regions of charge accumulation appear in the molecule. These charge accumulation regions in the molecule are near the locations of the O and N ions, which in **Confs. 2 and 4** are closer to graphene than in **Confs. 1 and 3**, and act as electron sinks due to their high electronegativity. For this reason, **Confs. 2 and 4** have a lower charge transfer, as evidenced in Table 2. Transport measurements revealed higher electron transfer from the deposited compound **2** than from compound **1** to graphene, which might indicate that orientations with low electron transfer are preferred in compound **1**. Notably, higher or lower charge transfer is not correlated with higher or lower binding energy between a molecule and substrate.

Table 3 Spin Hamiltonian parameters found by CASSCF-NEVPT2 for each system, compared to the experimental results obtained by HF-ESR and DC magnetometry

System	D (cm^{-1})	E/D	g_x	g_y	g_z	g_{iso}
1 XRD (exp.)[a]	−25.3	0.084	2.185	2.126	2.462	2.258
1 Isolated[b]	−18.5	0.009	2.139	2.141	2.368	2.216
1 Conf. 1[b]	−18.5	0.011	2.139	2.142	2.368	2.216
1 Conf. 2[b]	−18.6	0.014	2.139	2.143	2.370	2.217
1 Conf. 3[b]	−18.4	0.010	2.139	2.141	2.367	2.216
1 Conf. 4[b]	−18.4	0.016	2.139	2.144	2.368	2.217
1 HF-ESR	<-20	0.122	2.20	2.15	2.40	2.25
1 DC magn	−15.3	0.012	—	—	—	2.272
2 XRD (exp.)[a]	−28.3	0.107	2.201	2.119	2.501	2.274
2 Isolated[b]	−18.2	0.040	2.129	2.152	2.364	2.215
2 Conf. 1[b]	−18.9	0.030	2.131	2.151	2.373	2.218
2 Conf. 2[b]	−18.5	0.033	2.131	2.151	2.368	2.217
2 Conf. 3[b]	−18.4	0.038	2.129	2.152	2.367	2.216
2 Conf. 4[b]	−19.2	0.034	2.131	2.152	2.378	2.220
2 DC magn.	−17.5	0.044	—	—	—	2.213

[a] CASSCF-NEVPT2 def2-TZVP method in ORCA 5.0. [b] CASSCF-NEVPT2 def2-TZVP method in ORCA 4.2.1.

We focus now on the ZFS terms and *g*-factors of the deposited structures, as calculated by CASSCF-NEVPT2 in ORCA 4.2.1. The results are summarized in Table 2. In all systems, we obtained a negative *D*, in agreement with DC magnetometry and HF-ESR measurements. Additionally, the calculations suggest an anisotropy of the *g*-factors before and after adsorption. Overall, a discrepancy between the calculated parameters for the bulk structures and the deposited configurations is found, which is more evident in the ZFS terms *D* and *E*. This result is a direct consequence of the geometrical changes in the molecule in the gas phase after DFT relaxation. Furthermore, the parameters of the isolated and adsorbed molecules are practically the same in both compounds due to the negligible geometrical change after deposition.

4 Conclusions and outlook

We have presented a theoretical and experimental study on the structure, stability, magnetic properties, and deposition properties on graphene of compounds **1** and **2**. DFT calculations and analysis of the topology of the electron density by QT-AIM confirmed that the Co center and the pyridyne nitrogens N2 interact through attractive non-covalent interactions, thus exhibiting a semi-coordination character. We claim that such interaction is the source of the stability of the complexes under ambient conditions and after deposition on graphene, as confirmed by XPS and Raman spectroscopy. DC magnetometry showed that the compounds

present an axial magnetic anisotropy, with an axial ZFS term of $D = -15.3\ cm^{-1}$ and $-17.5\ cm^{-1}$ for **1** and **2**, respectively, while HF-ESR set the bound $|D| > 20\ cm^{-1}$ on compound **1**. Both experimental methods confirm a weak intermolecular antiferromagnetic exchange interaction, in agreement with BS-DFT predictions. Dynamic magnetic investigations confirmed that the compounds are field-induced SIMs with maximum relaxation times of 2.3 ms (at 0.06 *T*, 1.9 K) and 1.5 ms (at 0.09 *T*, 1.9 K) for **1** and **2**, respectively. Theoretical modeling of the compounds on graphene by DFT shows an attractive interaction between them with a relatively small binding energy, with the highest one (in absolute value) corresponding to −1.15 eV per molecule for compound **2** in **Conf. 4**. DOS and charge transfer analysis revealed an electron transfer from the molecule's HOMO to graphene, confirmed by transport measurements on GFETs and Raman spectroscopy, which increases the molecules' magnetic moment due to an increase in their spin density. This suggests the possibility of tuning the molecule's magnetic moment by electrostatic gating of the graphene substrate, which could be done by depositing them directly onto graphene quantum dot bolometers,[54,55] taking advantage of their high sensitivity that enables an *in situ* spectroscopic investigation.

Author contributions

Writing original draft preparation, plane-wave DFT, CASSCF-NEVPT2 calculations, J. N. G.; writing original draft preparation, XPS, depositions, J. H.; AFM, Raman, and depositions, Š. V.; chemical synthesis and analytical characterization of ligand and complex, O. F. F.; DC magnetometry experiments and preliminary analysis, L. H.; deposition on GFETs, transport measurements, D. H.; GFETs fabrication, S. d. S.; BS-DFT, CASSCF-NEVPT2 calculations, R. H.; graphene sample preparation, M. B.; AC magnetometry analysis, writing original draft preparation, I. Š.; HF-ESR experiments and analysis, V. T. S.; transport measurements, GFETs fabrication, supervision, P. B.; XRD analysis, DFT-topology and ELF calculations, DC magnetometry analysis, writing review and editing, I. N.; supervision, P. N. All authors have agreed to the published version of the manuscript.

Conflicts of interest

There are no conflicts to declare.

Acknowledgements

We gratefully acknowledge the projects and grant agencies that supported this work. O. F. F., R. H., and I. N. acknowledge support from the Grant Agency of the Czech Republic (GAČR 23-07175S); J. N. G. acknowledges the Grant Agency of the Czech Republic (GAČR 23-05578S), a student grant of the Brno University of Technology (CEITEC-J-21-7508), and the Brno PhD Talent Scholarship – Funded by the Brno City Municipality; J. N. G., J. H., and L. H. acknowledge the MEYS CR INTER-EXCELLENCE Programme (grant LTAUSA19060); O. F. F. acknowledges Palacky University's student grant DSGC-2021-0032 financed from the funds of the Operational Program Research, Development and Education under the project ''Improving schematics of Doctoral student grant competition and their pilot implementation'', Reg. No. CZ.02.2.69/0.0/0.0/19_ 073/0016713; M. B. acknowledges funding from the ESF under the project CZ.02.2.69/0.0/0.0/20_079/0017436; I. Š. acknowledges the grants from Slovak grant agencies DS-FR-22-0010, APVV-22-0172, APVV-19-0087, VEGA 1/0029/22; V. T. S. acknowledges funding from the EXPRO grant of the Grant Agency of the Czech Republic (GAČR 21-20716X); P. N. acknowledges the ERC Starting Grant (No. 714850) under the European Unions Horizon 2020 Research and Innovation Program. J. N. G., J. H., Š. V., and L. H. gratefully acknowledge the CzechNanoLab Research Infrastructure supported by MEYS CR (LM2018110). This article was written thanks to generous support through the Operational Program Integrated Infrastructure for the project: ''Strategic research in the field of SMART monitoring, treatment and preventive protection against coronavirus (SARS-CoV-2)'', Project No. 313011ASS8, co-financed by the European Regional Development Fund.

Notes and references

1 D. Tanaka, N. Aketa, H. Tanaka, S. Horike, M. Fukumori, T. Tamaki, T. Inose, T. Akai, H. Toyama, O. Sakata, H. Tajiri and T. Ogawa, *Dalton Trans.*, 2019, **48**, 7074–7079.
2 A. Ardavan, O. Rival, J. J. Morton, S. J. Blundell, A. M. Tyryshkin, G. A. Timco and R. E. Winpenny, *Phys. Rev. Lett.*, 2007, **98**, 057201.
3 M. Urdampilleta, S. Klyatskaya, J. P. Cleuziou, M. Ruben and W. Wernsdorfer, *Nat. Mater.*, 2011, **10**, 502–506.
4 E. Coronado, *Nat. Rev. Mat.*, 2020, **5**, 87–104.
5 J. Dugay, M. Aarts, M. Gimenez-Marqués, T. Kozlova, H. W. Zandbergen, E. Coronado and H. S. Van Der Zant, *Nano Lett.*, 2017, **17**, 186–193.
6 T. S. Rahman, R. S. Berkley, Z. Hooshmand, T. Jiang, D. Le and A. F. Hebard, *J. Phys. Chem. C*, 2020, **124**, 28186–28200.
7 R. J. Holmberg and M. Murugesu, *J. Mater. Chem. C*, 2015, **3**, 11986–11998.
8 P. C. Bunting, M. Atanasov, E. Damgaard-Møller, M. Perfetti, I. Crassee, M. Orlita, J. Overgaard, J. Van Slageren, F. Neese and J. R. Long, *Science*, 2018, **362**, eaat7319.
9 F. Yang, Q. Zhou, Y. Zhang, G. Zeng, G. Li, Z. Shi, B. Wang and S. Feng, *Chem. Commun.*, 2013, **49**, 5289–5291.
10 T. Wu, Y. Q. Zhai, Y. F. Deng, W. P. Chen, T. Zhang and Y. Z. Zheng, *Dalton Trans.*, 2019, **48**, 15419–15426.
11 M. Böhme, S. Ziegenbalg, A. Aliabadi, A. Schnegg, H. Görls and W. Plass, *Dalton Trans.*, 2018, **47**, 10861–10873.
12 S. Vaidya, P. Shukla, S. Tripathi, E. Rivière, T. Mallah, G. Rajaraman and M. Shanmugam, *Inorg. Chem.*, 2018, **57**, 3371–3386.
13 Y. Q. Zhai, Y. F. Deng and Y. Z. Zheng, *Dalton Trans.*, 2018, **47**, 8874–8878.

14 T. Jurca, A. Farghal, P. H. Lin, I. Korobkov, M. Murugesu and D. S. Richeson, *J. Am. Chem. Soc.*, 2011, **133**, 15814–15817.
15 I. Nemec, H. Liu, R. Herchel, X. Zhang and Z. Trávníček, *Synth. Met.*, 2016, **215**, 158–163.
16 R. Ruamps, L. J. Batchelor, R. Guillot, G. Zakhia, A. L. Barra, W. Wernsdorfer, N. Guihéry and T. Mallah, *Chem. Sci.*, 2014, **5**, 3418–3424.
17 D. Schweinfurth, J. Krzystek, M. Atanasov, J. Klein, S. Hohloch, J. Telser, S. Demeshko, F. Meyer, F. Neese and B. Sarkar, *Inorg. Chem.*, 2017, **56**, 5253–5265.
18 D. Schweinfurth, M. G. Sommer, M. Atanasov, S. Demeshko, S. Hohloch, F. Meyer, F. Neese and B. Sarkar, *J. Am. Chem. Soc.*, 2015, **137**, 1993–2005.
19 F. El-Khatib, B. Cahier, F. Shao, M. López-Jordà, R. Guillot, E. Rivière, H. Hafez, Z. Saad, J. J. Girerd, N. Guihéry and T. Mallah, *Inorg. Chem.*, 2017, **56**, 4601–4608.
20 J. Juráková, J. Dubnická Midlíková, J. Hrubý, A. Kliuikov, V. T. Santana, J. Pavlik, J. Moncol, E. Čižmár, M. Orlita, I. Mohelský, P. Neugebauer, D. Gentili, M. Cavallini and I. Šalitroš, *Inorg. Chem. Front.*, 2022, **9**, 1179–1194.
21 V. V. Novikov, A. A. Pavlov, Y. V. Nelyubina, M. E. Boulon, O. A. Varzatskii, Y. Z. Voloshin and R. E. Winpenny, *J. Am. Chem. Soc.*, 2015, **137**, 9792–9795.
22 A. A. Pavlov, Y. V. Nelyubina, S. V. Kats, L. V. Penkova, N. N. Efimov, A. O. Dmitrienko, A. V. Vologzhanina, A. S. Belov, Y. Z. Voloshin and V. V. Novikov, *J. Phys. Chem. Lett.*, 2016, **7**, 4111–4116.
23 S. Gomez-Coca, E. Cremades, N. Aliaga-Alcalde and E. Ruiz, *J. Am. Chem. Soc.*, 2013, **135**, 7010–7018.
24 T. J. Ozumerzifon, I. Bhowmick, W. C. Spaller, A. K. Rappé and M. P. Shores, *Chem. Commun.*, 2017, **53**, 4211–4214.
25 B. Yao, Y. F. Deng, T. Li, J. Xiong, B. W. Wang, Z. Zheng and Y. Z. Zhang, *Inorg. Chem.*, 2018, **57**, 14047–14051.
26 Y. Y. Zhu, C. Cui, Y. Q. Zhang, J. H. Jia, X. Guo, C. Gao, K. Qian, S. D. Jiang, B. W. Wang, Z. M. Wang and S. Gao, *Chem. Sci.*, 2013, **4**, 1802–1806.
27 B. Yao, M. K. Singh, Y. F. Deng, Y. N. Wang, K. R. Dunbar and Y. Z. Zhang, *Inorg. Chem.*, 2020, **59**, 8505–8513.
28 J. M. Frost, K. L. Harriman and M. Murugesu, *Chem. Sci.*, 2016, **7**, 2470–2491.
29 J. Juráková and I. Šalitroš, *Monatsh. Chem.*, 2022, **153**, 1001–1036.
30 J. M. Zadrozny and J. R. Long, *J. Am. Chem. Soc.*, 2011, **133**, 20732–20734.
31 E. A. Suturina, J. Nehrkorn, J. M. Zadrozny, J. Liu, M. Atanasov, T. Weyhermüller, D. Maganas, S. Hill, A. Schnegg, E. Bill, J. R. Long and F. Neese, *Inorg. Chem.*, 2017, **56**, 3102–3118.
32 J. M. Zadrozny, J. Telser and J. R. Long, *Polyhedron*, 2013, **64**, 209–217.
33 S. Vaidya, S. Tewary, S. K. Singh, S. K. Langley, K. S. Murray, Y. Lan, W. Wernsdorfer, G. Rajaraman and M. Shanmugam, *Inorg. Chem.*, 2016, **55**, 9564–9578.
34 M. S. Fataftah, J. M. Zadrozny, D. M. Rogers and D. E. Freedman, *Inorg. Chem.*, 2014, **53**, 10716–10721.
35 Y. Rechkemmer, F. D. Breitgoff, M. Van Der Meer, M. Atanasov, M. Hakl, M. Orlita, P. Neugebauer, F. Neese, B. Sarkar and J. Van Slageren, *Nat. Commun.*, 2016, **7**, 1–8.
36 S. Ziegenbalg, D. Hornig, H. Görls and W. Plass, *Inorg. Chem.*, 2016, **55**, 4047–4058.
37 X. N. Yao, M. W. Yang, J. Xiong, J. J. Liu, C. Gao, Y. S. Meng, S. D. Jiang, B. W. Wang and S. Gao, *Inorg. Chem. Front.*, 2017, **4**, 701–705.
38 J. Hrubý, Š. Vavrečková, L. Masaryk, A. Sojka, J. Navarro-Giraldo, M. Bartoš, R. Herchel, J. Moncol, I. Nemec and P. Neugebauer, *Molecules*, 2020, **25**, 5021.
39 J. Hrubý, D. Dvořák, L. Squillantini, M. Mannini, J. Van Slageren, R. Herchel, I. Nemec and P. Neugebauer, *Dalton Trans.*, 2020, **49**, 11697–11707.
40 I. Nemec, O. F. Fellner, L. Havlíček and R. Herchel, *Acta Crystallogr., Sect. A: Found. Adv.*, 2021, **77**, C344.
41 L. Xu, Y. V. Mironov, X. Qi and S. J. Kim, *J. Struct. Chem.*, 2006, **47**, 998–1001.
42 C. R. Groom, I. J. Bruno, M. P. Lightfoot and S. C. Ward, *Acta Crystallogr. B*, 2016, **72**, 171–179.
43 Z. M. Efimenko, A. S. Novikov, D. M. Ivanov, A. V. Piskunov, A. A. Vereshchagin, O. V. Levin, N. A. Bokach and V. Y. Kukushkin, *Inorg. Chem.*, 2020, 2316–2327.
44 I. V. Ananyev, N. A. Bokach and V. Y. Kukushkinc, *Acta Crystallogr., Sect. B: Struct. Sci., Cryst. Eng. Mater.*, 2020, **76**, 436–449.
45 L. J. Bourhis, O. V. Dolomanov, R. J. Gildea, J. A. Howard and H. Puschmann, *Acta Crystallogr., Sect. A: Found. Adv.*, 2015, **71**, 59–75.
46 G. M. Sheldrick, *Acta Crystallogr., Sect. C: Struct. Chem.*, 2015, **71**, 3–8.
47 O. V. Dolomanov, L. J. Bourhis, R. J. Gildea, J. A. Howard and H. Puschmann, *J. Appl. Crystallogr.*, 2009, **42**, 339–341.
48 C. F. MacRae, I. Sovago, S. J. Cottrell, P. T. Galek, P. McCabe, E. Pidcock, M. Platings, G. P. Shields, J. S. Stevens, M. Towler and P. A. Wood, *J. Appl. Crystallogr.*, 2020, **53**, 226–235.
49 A. K. Geim and K. S. Novoselov, *Nat. Mater.*, 2007, **6**, 183–191.
50 X. Du, I. Skachko, E. Y. Andrei and A. Barker, *Nat. Nanotechnol.*, 2008, **3**, 491–495.
51 C. Lee, X. Wei, J. W. Kysar and J. Hone, *Science*, 2008, **321**, 385–388.
52 J. H. Seol, I. Jo, A. L. Moore, L. Lindsay, Z. H. Aitken, M. T. Pettes, X. Li, Z. Yao, R. Huang, D. Broido, N. Mingo, R. S. Ruoff and L. Shi, *Science*, 2010, **328**, 213–216.
53 P. Neugebauer, M. Orlita, C. Faugeras, A. L. Barra and M. Potemski, *Phys. Rev. Lett.*, 2009, **103**, 136403.
54 A. El Fatimy, R. L. Myers-Ward, A. K. Boyd, K. M. Daniels, D. K. Gaskill and P. Barbara, *Nat. Nanotechnol.*, 2016, **11**, 335–338.
55 L. S. Marie, A. El Fatimy, J. Hrubý, I. Nemec, J. Hunt, R. Myers-Ward, D. K. Gaskill, M. Kruskopf, Y. Yang, R. Elmquist, R. Marx, J. van Slageren, P. Neugebauer and P. Barbara, *J. Phys. Mater.*, 2020, **3**, 014013.

56 B. Zhan, C. Li, J. Yang, G. Jenkins, W. Huang and X. Dong, *Small*, 2014, **10**, 4042–4065.
57 F. Neese, *Wiley Interdiscip. Rev. Comput. Mol. Sci.*, 2018, **8**, e1327.
58 F. Neese, *Wiley Interdiscip. Rev. Comput. Mol. Sci.*, 2022, **12**, e1606.
59 P. Å. Malmqvist and B. O. Roos, *Chem. Phys. Lett.*, 1989, **155**, 189–194.
60 C. Angeli, R. Cimiraglia, S. Evangelisti, T. Leininger and J. P. Malrieu, *J. Chem. Phys.*, 2001, **114**, 10252.
61 C. Angeli, R. Cimiraglia and J. P. Malrieu, *Chem. Phys. Lett.*, 2001, **350**, 297–305.
62 F. Kleemiss, O. V. Dolomanov, M. Bodensteiner, N. Peyerimhoff, L. Midgley, L. J. Bourhis, A. Genoni, L. A. Malaspina, D. Jayatilaka, J. L. Spencer, F. White, B. Grundkötter-Stock, S. Steinhauer, D. Lentz, H. Puschmann and S. Grabowsky, *Chem. Sci.*, 2021, **12**, 1675–1692.
63 F. Weigend and R. Ahlrichs, *Phys. Chem. Chem. Phys.*, 2005, **7**, 3297–3305.
64 F. Weigend, *Phys. Chem. Chem. Phys.*, 2006, **8**, 1057–1065.
65 A. Hellweg, C. Hättig, S. Höfener and W. Klopper, *Theor. Chem. Acc.*, 2007, **117**, 587–597.
66 R. Izsák and F. Neese, *J. Chem. Phys.*, 2011, **135**, 144105.
67 F. Neese, F. Wennmohs, A. Hansen and U. Becker, *Chem. Phys.*, 2009, **356**, 98–109.
68 *Molecular Electronic Structures of Transition Metal Complexes II*, ed. D. M. P. Mingos, P. Day and J. P. Dahl, Springer Berlin Heidelberg, Berlin, Heidelberg, 2012, vol. 143.
69 A. D. Becke, *Phys. Rev. A: At., Mol., Opt. Phys.*, 1988, **38**, 3098–3100.
70 C. Lee, W. Yang and R. G. Parr, *Phys. Rev. B: Condens. Matter Mater. Phys.*, 1988, **37**, 785–789.
71 P. J. Stephens, F. J. Devlin, C. F. Chabalowski and M. J. Frisch, *J. Phys. Chem.*, 1994, **98**, 11623–11627.
72 C. Adamo and V. Barone, *J. Chem. Phys.*, 1999, **110**, 6158–6170.
73 S. M. Hossain, S. Kamilya, S. Ghosh, R. Herchel, M. A. Kiskin, S. Mehta and A. Mondal, *Cryst. Growth Des.*, 2023, **11**, 42.
74 L. Havlíček, R. Herchel, I. Nemec and P. Neugebauer, *Polyhedron*, 2022, **223**, 115962.
75 A. N. Gusev, I. Nemec, R. Herchel, Y. I. Baluda, M. A. Kryukova, N. N. Efimov, M. A. Kiskin and W. Linert, *Polyhedron*, 2021, **196**, 115017.
76 A. Bhanja, L. Smythe, R. Herchel, I. Nemec, M. Murrie and D. Ray, *Dalton Trans.*, 2021, **50**, 5023–5035.
77 B. Rybníčková, J. Kuchár, P. Antal and R. Herchel, *Inorg. Chim. Acta*, 2020, **509**, 119689.
78 I. Šalitroš, R. Herchel, O. Fuhr, R. González-Prieto and M. Ruben, *Inorg. Chem.*, 2019, **58**, 4310–4319.
79 O. A. Vydrov and T. Van Voorhis, *J. Chem. Phys.*, 2010, **133**, 244103.
80 W. Hujo and S. Grimme, *J. Chem. Theory Comput.*, 2011, **7**, 3866–3871.
81 R. F. W. Bader, *Atoms in Molecules: A Quantum Theory*, Oxford University Press, 1994.
82 T. Lu and F. Chen, *J. Mol. Graphics Modell.*, 2012, **38**, 314–323.
83 T. Lu and F. Chen, *J. Comput. Chem.*, 2012, **33**, 580–592.
84 G. Kresse and J. Hafner, *Phys. Rev. B: Condens. Matter Mater. Phys.*, 1993, **47**, 558–561.
85 G. Kresse and J. Furthmüller, *Computational Mater. Sci.*, 1996, **6**, 15–50.
86 G. Kresse and J. Furthmüller, *Phys. Rev. B: Condens. Matter Mater. Phys.*, 1996, **54**, 11169–11186.
87 G. Kresse and D. Joubert, *Phys. Rev. B: Condens. Matter Mater. Phys.*, 1999, **59**, 1758–1775.
88 P. E. Blöchl, *Phys. Rev. B: Condens. Matter Mater. Phys.*, 1994, **50**, 17953–17979.
89 J. P. Perdew, K. Burke and M. Ernzerhof, *Phys. Rev. Lett.*, 1996, **77**, 3865–3868.
90 J. P. Perdew, K. Burke and M. Ernzerhof, *Phys. Rev. Lett.*, 1997, **78**, 1396.
91 S. Grimme, J. Antony, S. Ehrlich and H. Krieg, *J. Chem. Phys.*, 2010, **132**, 154709.
92 S. Grimme, S. Ehrlich and L. Goerigk, *J. Comput. Chem.*, 2011, **32**, 1456–1465.
93 J. Neugebauer and M. Scheffler, *Phys. Rev. B: Condens. Matter Mater. Phys.*, 1992, **46**, 16067–16080.
94 G. Makov and M. C. Payne, *Phys. Rev. B: Condens. Matter Mater. Phys.*, 1995, **51**, 4014–4022.
95 H. J. Monkhorst and J. D. Pack, *Phys. Rev. B: Solid State*, 1976, **13**, 5188–5192.
96 V. Wang, N. Xu, J.-C. Liu, G. Tang and W.-T. Geng, *Comput. Phys. Commun.*, 2021, **267**, 108033.
97 K. Momma and F. Izumi, *J. Appl. Crystallogr.*, 2008, **41**, 653–658.
98 E. R. Johnson, S. Keinan, P. Mori-Sánchez, J. Contreras-García, A. J. Cohen and W. Yang, *J. Am. Chem. Soc.*, 2010, **132**, 6498–6506.
99 W. Humphrey, A. Dalke and K. Schulten, *J. Mol. Graphics*, 1996, **14**, 33–38.
100 A. D. Becke and K. E. Edgecombe, *J. Chem. Phys.*, 1990, **92**, 5397–5403.
101 T. Lu and F. W. Chen, *Acta Phys. Chim. Sin.*, 2011, **27**, 2786–2792.
102 Y. H. Chi, J. M. Shi, H. N. Li, W. Wei, E. Cottrill, N. Pan, H. Chen, Y. Liang, L. Yu, Y. Q. Zhang and C. Hou, *Dalton Trans.*, 2013, **42**, 15559–15569.
103 E. Ruiz, J. Cano, S. Alvarez and P. Alemany, *J. Comput. Chem.*, 1999, **20**, 1391–1400.
104 T. Soda, Y. Kitagawa, T. Onishi, Y. Takano, Y. Shigeta, H. Nagao, Y. Yoshioka and K. Yamaguchi, *Chem. Phys. Lett.*, 2000, **319**, 223–230.
105 S. Stoll and A. Schweiger, *J. Magn. Reson.*, 2006, **178**, 42–55.
106 E. Y. Misochko, A. V. Akimov, D. V. Korchagin, J. Nehrkorn, M. Ozerov, A. V. Palii, J. M. Clemente-Juan and S. M. Aldoshin, *Inorg. Chem.*, 2019, **58**, 16434–16444.
107 L. F. Chibotaru and L. Ungur, *J. Chem. Phys.*, 2012, **137**, 64112.

108 J. Yan, Y. Zhang, P. Kim and A. Pinczuk, *Phys. Rev. Lett.*, 2007, **98**, 166802.
109 A. C. Ferrari and D. M. Basko, *Nat. Nanotechnol.*, 2013, **8**, 235–246.
110 W. Tang, E. Sanville and G. Henkelman, *J. Phys.: Condens. Matter*, 2009, **21**, 084204.
111 G. Henkelman, A. Arnaldsson and H. Jónsson, *Comput. Mater. Sci.*, 2006, **36**, 354–360.

Volume 26
Number 8
28 February 2024
Pages 6461–7242

PCCP

Physical Chemistry Chemical Physics

rsc.li/pccp

25 YEARS ANNIVERSARY

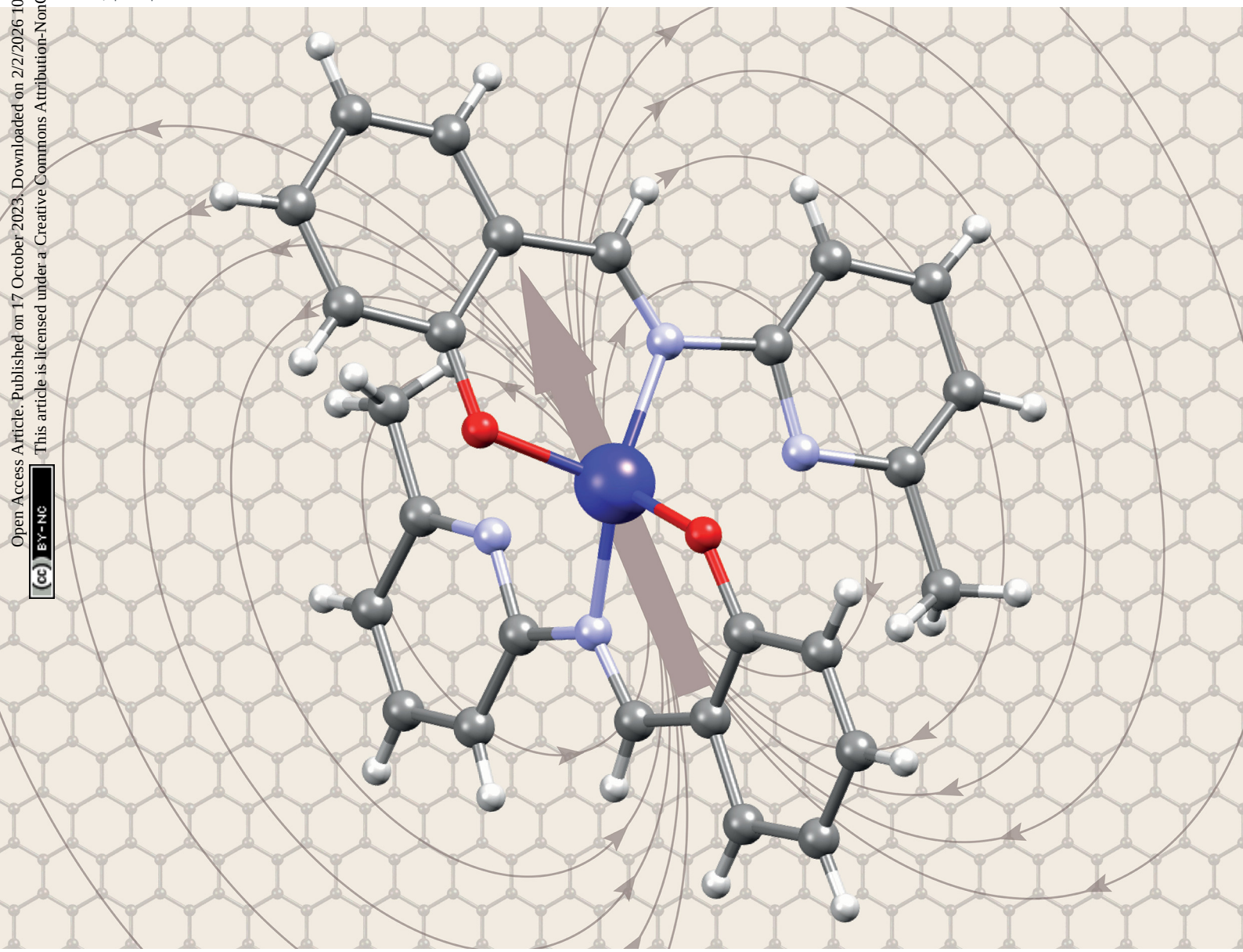

ISSN 1463-9076

ROYAL SOCIETY OF CHEMISTRY

PAPER

Ivan Nemec, Petr Neugebauer *et al.*

Tetracoordinate Co(II) complexes with semi-coordination as stable single-ion magnets for deposition on graphene

PCCP Owner Societies